



## Article

# Millimeter-Wave-to-Terahertz Superconducting Plasmonic Waveguides for Integrated Nanophotonics at Cryogenic Temperatures

Samane Kalhor<sup>1</sup>, Majid Ghanaatshoar<sup>1</sup>, Hannah J. Joyce<sup>2</sup> , David A. Ritchie<sup>3</sup>, Kazuo Kadowaki<sup>4</sup> and Kaveh Delfanazari<sup>2,3,5,\*</sup> 

<sup>1</sup> Laser and Plasma Research Institute, Shahid Beheshti University, Tehran 19839-69411, Iran; samane.kalhor@gmail.com (S.K.); m-ghanaat@sbu.ac.ir (M.G.)

<sup>2</sup> Electrical Engineering Division, University of Cambridge, Cambridge CB3 0FA, UK; hannah.joyce@eng.cam.ac.uk

<sup>3</sup> Department of Physics, Cavendish Laboratory, University of Cambridge, Cambridge CB3 0FA, UK; dar11@cam.ac.uk

<sup>4</sup> Division of Materials Science, Faculty of Pure & Applied Sciences, University of Tsukuba 1-1-1, Tennodai, Tsukuba, Ibaraki 305-8573, Japan; dr.kazuo.kadowaki@gmail.com

<sup>5</sup> James Watt School of Engineering, University of Glasgow, Glasgow G12 8QQ, UK

\* Correspondence: kaveh.delfanazari@glasgow.ac.uk



**Citation:** Kalhor, S.; Ghanaatshoar, M.; Joyce, H.J.; Ritchie, D.A.; Kadowaki, K.; Delfanazari, K. Millimeter-Wave-to-Terahertz Superconducting Plasmonic Waveguides for Integrated Nanophotonics at Cryogenic Temperatures. *Materials* **2021**, *14*, 4291. <https://doi.org/10.3390/ma14154291>

Academic Editor: Alexandros Lappas

Received: 8 June 2021

Accepted: 7 July 2021

Published: 31 July 2021

**Publisher's Note:** MDPI stays neutral with regard to jurisdictional claims in published maps and institutional affiliations.



**Copyright:** © 2021 by the authors. Licensee MDPI, Basel, Switzerland. This article is an open access article distributed under the terms and conditions of the Creative Commons Attribution (CC BY) license (<https://creativecommons.org/licenses/by/4.0/>).

**Abstract:** Plasmonics, as a rapidly growing research field, provides new pathways to guide and modulate highly confined light in the microwave-to-optical range of frequencies. We demonstrated a plasmonic slot waveguide, at the nanometer scale, based on the high-transition-temperature ( $T_c$ ) superconductor  $\text{Bi}_2\text{Sr}_2\text{CaCu}_2\text{O}_{8+\delta}$  (BSCCO), to facilitate the manifestation of chip-scale millimeter wave (mm-wave)-to-terahertz (THz) integrated circuitry operating at cryogenic temperatures. We investigated the effect of geometrical parameters on the modal characteristics of the BSCCO plasmonic slot waveguide between 100 and 800 GHz. In addition, we investigated the thermal sensing of the modal characteristics of the nanoscale superconducting slot waveguide and showed that, at a lower frequency, the fundamental mode of the waveguide had a larger propagation length, a lower effective refractive index, and a strongly localized modal energy. Moreover, we found that our device offered a larger SPP propagation length and higher field confinement than the gold plasmonic waveguides at broad temperature ranges below BSCCO's  $T_c$ . The proposed device can provide a new route toward realizing cryogenic low-loss photonic integrated circuitry at the nanoscale.

**Keywords:**  $\text{Bi}_2\text{Sr}_2\text{CaCu}_2\text{O}_{8+\delta}$  quantum material; high-temperature superconductor; on-chip light sources and detectors; plasmonic waveguides; quantum emitters; THz integrated circuitry; cryogenic circuitry

## 1. Introduction

The high-transition-temperature ( $T_c$ ) superconducting  $\text{Bi}_2\text{Sr}_2\text{CaCu}_2\text{O}_{8+\delta}$  (BSCCO) intrinsic Josephson junctions (IJJs)-based THz emitters radiate intense, coherent, and continuous THz photons with frequencies ranging from 0.1 to 11 THz [1–28]. Such THz devices can also be used as surface current-sensitive detectors due to the unique electrostatics of the BSCCO quantum material. Therefore, BSCCO-based devices are valuable for many applications, including THz imaging, interferometry, and absorption measurement [29]. The design of low-loss mm-wave-to-THz components, e.g., waveguides, capable of being integrated with such superconducting emitters, and detectors, are vital to accomplishing all BSCCO-made chip-integrated mm-wave-to-THz circuitry. Moreover, the exploitation of superconducting quantum materials into the architectures of waveguides enables the implementation of the real-time sensing and controlling of waveguides, due to the sensitivity of the quantum mechanical phases of superconductors to external stimuli such as magnetic

fields, temperature, light, and current [30]. Cooper pairs in superconductors have an equivalent response to that of electrons in plasmonic metals at high frequencies [30]. Plasmonics deals with propagating surface plasmon polaritons (SPPs) such as the coupled oscillation of electrons and electromagnetic waves [31]. The innovative physical effect of plasmonic devices such as subwavelength localization of the electromagnetic field provides a new route in novel chip-scale integrated photonic devices [32–34]. In superconductors, the coherent oscillation of plasmonic waves is a result of the formation of Cooper pairs and the absence of scattering [35]. The surface plasmon oscillations in superconducting metals have been extensively investigated for single and multiple-film systems, and microstructure arrays [36–41]. It was shown that extraordinary transmission through a subwavelength hole array in a superconducting NbN film arises from the enhancement of SPPs below the transition temperature [39]. Moreover, it was demonstrated that the existence of superconducting plasmons in the YBCO subwavelength hole array is due to the dominance of kinetic resistance over inductance resistance in superconductors [40]. Furthermore, it was shown that  $\text{YBa}_2\text{Cu}_3\text{O}_7$  (YBCO) and niobium (Nb) plasmonic superconducting waveguides offer a superior long plasmon propagation distance in comparison to noble metals at THz frequencies [35,41] due to the intrinsic low-loss plasmonic properties of superconductors.

In this paper, we propose a mm-wave-to-THz superconducting plasmonic slot waveguide (PSW) based on BSCCO. We first studied the modal characteristics of the BSCCO PSW, including the effective refractive index, the propagation loss of SPPs, and mode energy confinement. Furthermore, we investigated thermal tuning of the modal characteristics of such waveguides at temperature ranges between  $T = 10$  and 100 K at the selected frequencies of  $f = 0.1, 0.3, 0.5,$  and  $0.8$  THz. The proposed waveguide can be integrated with BSCCO-based THz sources and detectors. It is also suitable for various applications such as tunable modulators and photodetectors.

## 2. Structure Design and Methods

A 3D schematic of the proposed BSCCO PSW is shown in Figure 1a. The cross-sectional view of the 3D SPW at the  $x$ - $z$  plane in Figure 1b shows that the waveguide consists of a deep subwavelength air slot of width  $w$  in a thin film of BSCCO with a thickness of  $h$ . The generated SPPs propagate through the air slot.

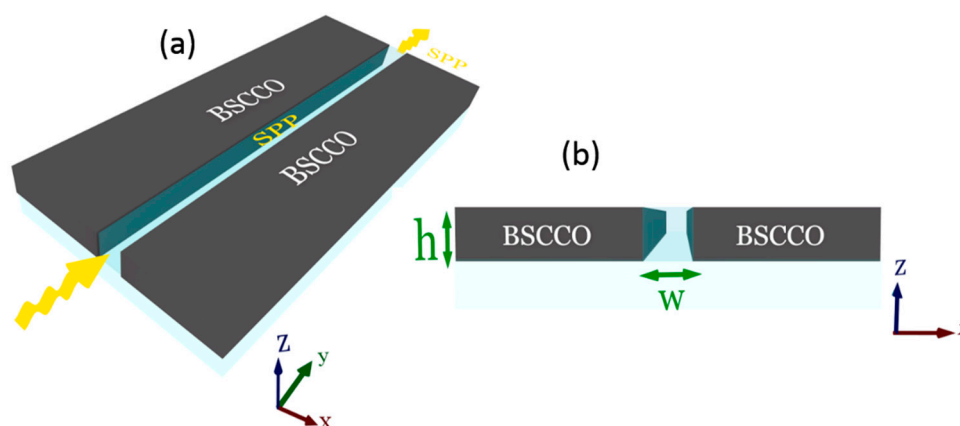


**Figure 1.** (a) Three-dimensional schematic diagram of the proposed suspended BSCCO-based plasmonic slot waveguide, (b) and the cross-sectional view of the waveguide at the  $x$ - $z$  plane.

We employed the numerical finite element simulation method (FEM)-based mode solver to calculate the eigenmodes of the plasmonic waveguide at a specific frequency  $\omega$ . Here, an  $\exp(-i\beta y)$  dependence for the electric field was considered because the waveguide is uniform along the  $y$ -direction [42]. Therefore, the electric field  $E$  distribution in the waveguide can be written as

$$E(x, y, z) = E(x, z) \exp(-i\beta y) \quad (1)$$

where  $\beta = \beta_1 + i\beta_2$  is the complex propagation constant of the waveguide's mode. The electromagnetic wave equation is defined as [43]

$$\nabla \times \nabla \times E = \frac{\omega^2}{c^2} \varepsilon E \quad (2)$$

where  $c$  is the speed of light in vacuum. For our waveguide whose structure is uniform in the  $y$ -direction, the wave equation reduces to [44]

$$\nabla_{\perp}^2 E + \left( \frac{\omega^2}{c^2} \varepsilon - \beta^2 \right) E = 0 \quad (3)$$

where we used the definition  $\nabla_{\perp}^2 = \partial^2 / \partial x^2 + \partial^2 / \partial z^2$ .

By calculating the eigenvalue of Equation (3), the propagation constant  $\beta$  is obtained. Then, the modal characteristics of the waveguide, including the real part of the effective refractive index ( $N_{eff}$ ) and propagation length ( $L_p$ ) of SPPs for the fundamental mode of the BSCCO PSW, can be calculated from equations [42,45]:

$$N_{eff} = \beta / k_0, \quad (4)$$

$$L_p = 1 / (2 \operatorname{Im}(\beta)), \quad (5)$$

where  $k_0$  is the free-space wavevector.  $N_{eff}$  is an indicator of the localization of SPP's energy and wavelength. In addition, the dispersion relation of the waveguide is defined as  $\omega = \omega(\beta)$  [42].

In Equation (2),  $\varepsilon$  is the permittivity of the relevant medium. The permittivity of air  $\varepsilon_{air}$  is 1, and the temperature- and frequency-dependent  $a$ - $b$  plane complex conductivity of BSCCO film with  $T_c = 85$  K is extracted from the experimental THz time-domain spectroscopy data [46–48]. The complex permittivity of BSCCO can be obtained from its complex conductivity [48].

For obtaining the eigenmode of the waveguide, the area of computation is considered large enough, and the perfectly-matched-layer (PML) absorbing boundary conditions are used along the  $x$ - and  $z$ -axis. Therefore, the reflection of fields from the boundaries is negligible. In addition, the factor of mode confinement is calculated as a ratio of power flow in the slot ( $w * h$  area) to the total power flow in the waveguide normal to the  $x$ - $z$  plane [45].

$$\Gamma = \frac{\int_{slot} \operatorname{Re}\{(E \times H^*) \cdot n\} dA}{\int_{total} \operatorname{Re}\{(E \times H^*) \cdot n\} dA} \quad (6)$$

where power flow is  $S_n = (1/2) \operatorname{Re}\{(E \times H^*) \cdot n\}$ . Here,  $E$  and  $H^*$  are the electric and complex conjugates of magnetic field vectors, respectively, and  $n$  is the normal unit vector in the  $y$ -direction.

### 3. Results and Discussion

The highest possible mode quality of the waveguide was obtained through optimization of the slot width  $w$  and BSCCO thin-film thickness  $h$  at the temperature  $T = 10$  K and frequency  $f = 0.1$  THz. The modal characteristics are controllable by the structural size of the waveguide. The effective refractive index ( $N_{eff}$ ) and propagation length ( $L_p$ ) of the BSCCO PSW as a function of BSCCO height  $h$  for different slot widths  $w$  are shown in Figure 2a,b.

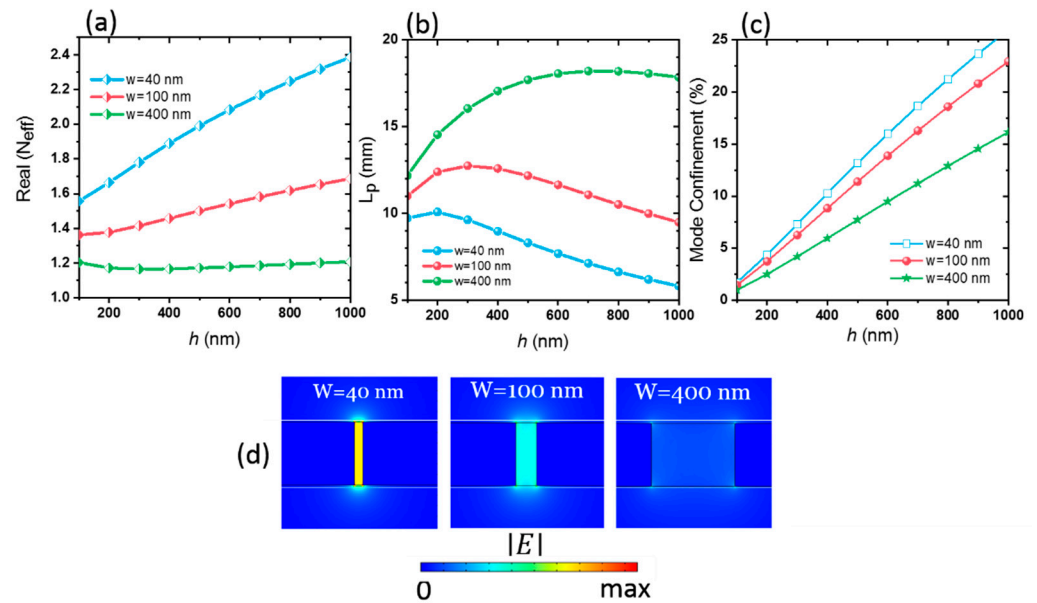


**Figure 2.** (a) Real part of the mode effective refractive index ( $N_{eff}$ ), (b) propagation length ( $L_p$ ), and (c) mode confinement of BSCCO THz plasmonic waveguide as a function of BSCCO thickness  $h$  for three slot widths of  $w = 40, 100,$  and  $400$  nm at  $f = 0.1$  THz and  $T = 10$  K. (d) Electric field distribution at slot widths of  $w = 40, 100,$  and  $400$  nm for BSCCO height  $h = 300$  nm. All field distributions curves have the same color bar.

At each BSCCO/air interface within the air gap, SPPs are formed. These two formed SPPs are coupled and create a transverse electromagnetic (TEM) wave mode.  $N_{eff}$  is larger than the air refractive index and is adjustable by the structural size. As  $h$  increases,  $N_{eff}$  increases, but  $L_p$  decreases because the superconductor/air interface height in the slot increases. The larger portion of BSCCO (whose  $N_{eff}$  is higher than air) results in a larger  $N_{eff}$ . Besides, as width  $w$  decreases,  $N_{eff}$  increases, and  $L_p$  reduces. Once the slot width is narrow, the SPP related to the two BSCCO surfaces form the coupled SPPs [49]. Therefore, as the  $w$  of the slot decreases, the propagation constant  $\beta$  increases and leads to the increase in  $N_{eff}$  and reduction in  $L_p$  [42]. The fall of  $L_p$  at very low  $h$  arises from the decoupling of two formed SPPs.

The mode confinement of SPPs is shown in Figure 2c. It determines the enhancement of energy in the slot region. The mode confinement reduces with increasing slot width  $w$ . To clarify this, we show the electric field distribution at different slot widths  $w$  for a constant  $h = 300$  nm in Figure 2d. We see that the slot width of  $w = 400$  nm has the lowest electric field distribution within the slot. Even though the narrower slot dimension has a large energy confinement, it suffers from the lower propagation length.

There is a tradeoff between the energy confinement of SPPs within the slot and SPP's propagation length. The largest  $L_p$  for SPW with thickness  $h = 300$  nm is for a slot width of  $w = 100$  nm. Hence, these values ( $w = 100$  nm and  $h = 300$  nm) were chosen as SPW optimum dimensions. Based on this optimization,  $N_{eff}$  is 1.42. The mode has a shorter wavelength in comparison to the free space. Therefore, the SPP's wavelength, which is defined as  $\lambda_0/N_{eff}$ , is 2.1 mm, and the SPP's field is confined in the air slot as small as  $\lambda_0^2/(3 \times 10^8)$ . Here,  $\lambda_0 = 3$  mm is the free-space wavelength. The propagation distance of SPPs is 12.73 mm, which is equal to six effective wavelengths.

The modal characteristics of the waveguide are dependent on the plasmonic properties of BSCCO.  $N_{eff}$ ,  $L_p$ , and mode confinement are shown in Figure 3a–c as a function of temperature for four different frequencies of  $f = 0.1, 0.3, 0.5,$  and  $0.8$  THz. For each frequency, it is found that  $N_{eff}$  reduces but  $L_p$  and mode confinement increase significantly as BSCCO enters the superconducting state below  $T_c$  (the vertical dashed line). The magnitude of the real part of BSCCO permittivity ( $|\epsilon_1|$ ) increases below  $T_c$  (see Figure 3d). The continuity of

the normal component of the electric field displacement ( $D$ ) at the boundary of the BSCCO and air interface as  $\varepsilon_{BSCCO}E_{BSCCO \perp} = \varepsilon_{air}E_{air \perp}$  results in the decrease in the electric field in BSCCO, by increasing  $|\varepsilon_1|$ , due to the material temperature reduction. Here,  $\varepsilon_{BSCCO}$  and  $\varepsilon_{air}$  are the permittivities of BSCCO and air, respectively.  $E_{1\perp}$  and  $E_{2\perp}$  are normal components of the electric field in BSCCO and air, respectively. The electric field reduction in the BSCCO results in a lower modal propagation constant  $\beta$  and lower  $N_{eff}$ . The growth in  $L_p$  and mode confinement with the cooling of the waveguide is also the outcome of lower  $\beta$ .

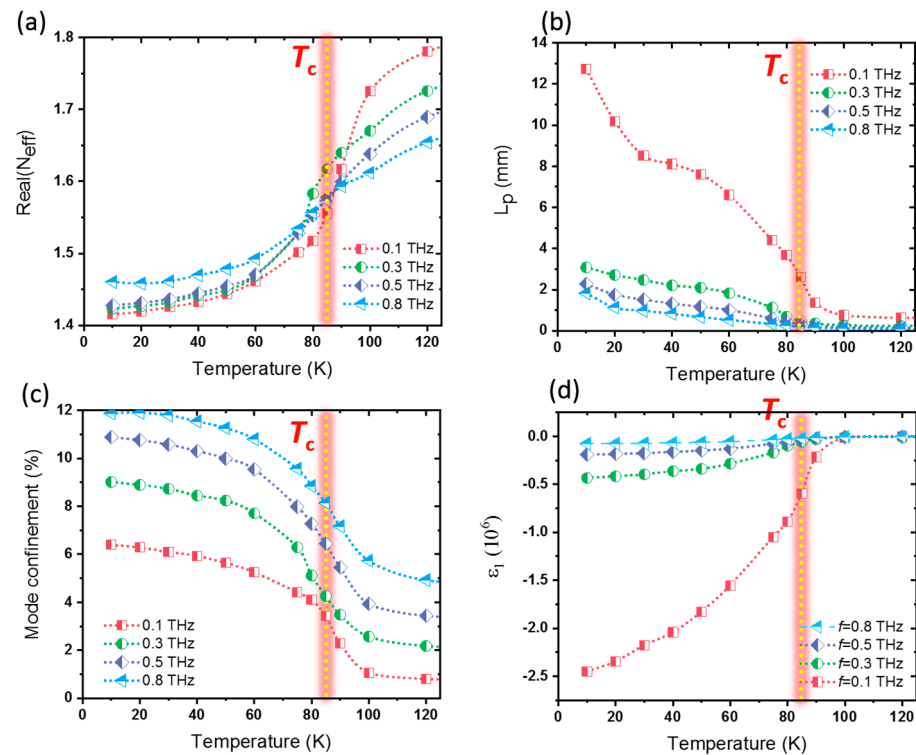


**Figure 3.** (a) Real part of the mode effective refractive index ( $N_{eff}$ ), (b) propagation length of SPPs ( $L_p$ ), (c) the mode confinement of the PSW as a function of temperature, and (d) the real part of BSCCO permittivity at different frequencies. The vertical dashed lines show the  $T_c$  of BSCCO.

Figure 3d shows the real part of the BSCCO permittivity at different frequencies. Indeed, superconductors are intrinsically plasmonic media with a negative real part of complex permittivity. Superconductor plasmonic properties are determined by the coexistence of normal and superconducting plasma. Normal carriers are responsible for scattering processes. At  $T_c$  and above, all carriers are in the normal phase. With a reduction in temperature to below  $T_c$ , the ratio of superconducting carriers to normal carriers increases. At zero temperature, all carriers turn into supercarriers according to the well-known two-fluid model [40,50]. Above  $T_c$  (vertical dashed line in Figure 3d) in the normal state of BSCCO,  $\varepsilon_1$  has a very low value. The material is nevertheless in the plasmonic regime, with a significant loss. At cryogenic temperatures below  $T_c$  of BSCCO, the absolute value of  $\varepsilon_1$  increases. Therefore, loss of the material decreases due to the growth of supercarrier densities. The growth of SPP's propagation length by reducing the temperature in Figure 3b is a result of loss reduction in BSCCO below  $T_c$ .

From Figure 3a–c, it could also be found that  $N_{eff}$  increases and  $L_p$  decreases with frequency. The growth in  $N_{eff}$  (Figure 3a) is due to the reduction in the absolute value of the real part of BSCCO permittivity with frequency (see Figure 3d), and also the larger penetration of mode power in BSCCO. Larger modal penetration in BSCCO means lower mode confinement within the slot (see Figure 3c). The reduction in  $L_p$  with frequency in Figure 3b is a result of the increasing Ohmic loss and also due to the larger fraction of the



modal power in BSCCO. However, there are less prominent differences between waveguide characteristics below and above the transition temperature at higher frequencies. This is first due to the increase in loss rate at higher frequencies. Moreover, in BSCCO, the two-fluid model cannot explain the low-frequency conductivity, as well as that of other layered superconductors such as YBCO with less anisotropy. In BSCCO, as an anisotropic cuprate, there is an additional spectral weight at low frequencies that increases as the material is cooled toward zero. This residual spectral weight (the so-called collective mode) arises from the fluctuation in the condensate order parameters [46–48] and draws about 30% of the spectral weight from the condensate [46]. However, there is good agreement between the BSCCO conductivity and the two-fluid model at higher frequencies.

For clarifying the effect of temperature, the dispersion relation of the mode of BSCCO PSW is shown in Figure 4a. Compared to the light line (dispersion relation of vacuum, shown with red color), it infers that the waveguide supports a bound mode because the waveguide lines are on the right side of the light line [51]. With the reduction in temperature, the slope of the curves becomes sharper. Therefore, cooling the waveguide results in reducing the refractive index. Lower  $N_{eff}$  for lower temperature dictates shorter SPP wavelengths. Moreover, the dispersion curves show that the energy is less confined at lower frequencies due to approaching the light line.

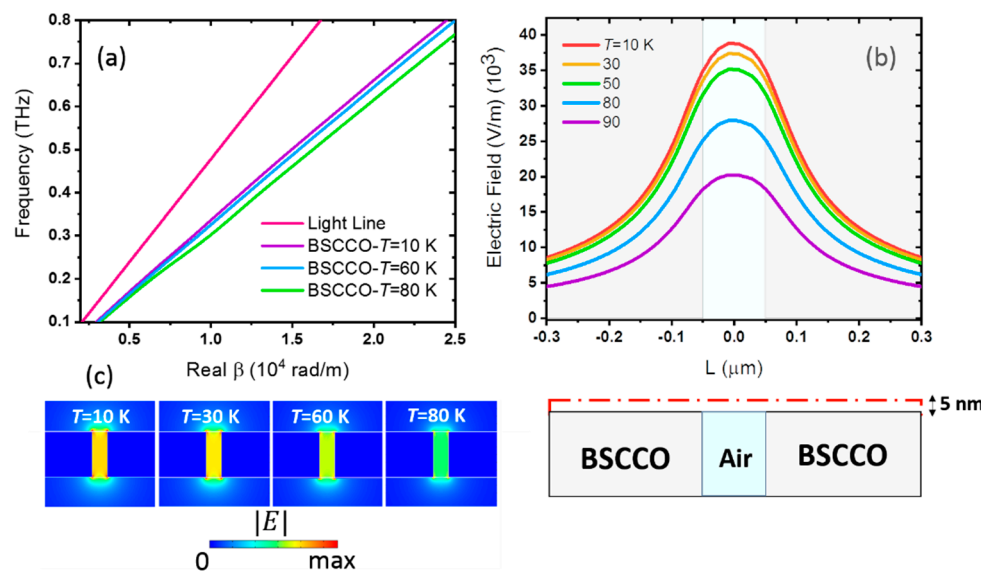


**Figure 4.** (a) Dispersion curves for the mode of the BSCCO PSW at  $T = 10$  K (purple),  $T = 60$  K (blue), and  $T = 80$  K (green). The red line shows the dispersion relation of the THz waves propagating in free space. (b) Electric field intensity at the red dashed line 5 nm above the waveguide, at different temperatures between  $T = 10$  and 90 K, at  $f = 0.1$  THz. The cross-section of the waveguide shows the relative position of the BSCCO film and the slot area in the electric field curves. The pale blue area shows the gap, while the grey area shows the BSCCO part. (c) The electric field distribution of the BSCCO THz PSW for width  $w = 100$  nm and height  $h = 300$  nm at  $f = 0.1$  THz for selected temperatures  $T = 10, 60,$  and  $80$  K. All field distributions have the same color bar.

For further investigation of the thermal tuning of confinement of the modal energy within the slot, the electric field distribution at 5 nm above the waveguide's surface along the dashed line is shown in the bottom panel of Figure 4b, for selected temperatures, at  $f = 0.1$  THz, and for the optimized waveguide size. Here, the top curve is aligned vertically with respect to the cross-sectional view of the waveguide. The pale blue area in the schematic of the waveguide and within the curve of Figure 4b shows the air slot area, while the grey area shows the BSCCO thin-film area. The electric field is enhanced within the slot for all temperatures, whereas it grows as temperature reduces due to the reduction

in the loss rate. The electric field distribution at different temperatures in Figure 4c also shows the enhancement of the field within the slot with the reduction in temperature.

The comparison between the BSCCO waveguide and gold waveguide with the same structural size of  $h = 300$  nm and  $w = 100$  nm at the frequency of  $f = 0.1$  THz shows that the BSCCO waveguide has a larger energy confinement and larger propagation length below  $T_c$  (see Figure A1). Therefore, the propagation characteristics of the proposed BSCCO waveguide are better than those of the gold waveguide below  $T_c$ . Above  $T_c$ , the propagation length of SPPs for the BSCCO waveguide is comparable to that of the gold plasmonic waveguide (see Figure A1 in Appendix A).

The absorption coefficient ( $\alpha$ ) of the waveguide can be calculated from  $\alpha = 2 \text{Imag}(\beta)$  [52]. The absorption coefficients of BSCCO and the gold plasmonic waveguide as a function of temperature and frequency are shown in Figure A2. For the BSCCO waveguide at the frequency of  $f = 0.1$  THz, the absorption coefficient is equal to 0.68 dB/mm at  $T = 10$  K and it increases to 3.34 dB/mm at  $T = 85$  K (the  $T_c$  of BSCCO). For gold, the absorption coefficient is as high as 6.85 dB/mm at the frequency of  $f = 0.1$  THz. Nevertheless, the absorption coefficient of the BSCCO waveguide is comparable to the gold waveguide above  $T_c$ . Additionally, the absorption confinement of both waveguides increases with frequency as a result of increasing Ohmic losses.

#### 4. Conclusions

We numerically investigated the temperature-dependent modal characteristics of a high- $T_c$  superconducting BSCCO plasmonic slot waveguide, including the refractive index, propagation length, and the mode confinement in the slot region at the mm-wave-to-THz range of frequencies. We showed that the propagation length of SPP increases as material enters the superconducting phase. In addition, we investigated the frequency tuning of the modal characteristics. Compared with the gold waveguide, the BSCCO waveguide at  $T = 10$  K offers higher mode confinement within the gap and a larger propagation length below  $T_c$ . The proposed BSCCO plasmonic waveguide helps realize a fully integrated BSCCO THz circuitry for applications in cryogenic on-chip quantum communication and low-loss data processing.

**Author Contributions:** Conceptualization, K.D.; methodology, K.D.; software, K.D. and S.K.; validation, K.D. and S.K.; formal analysis, S.K. and K.D.; investigation, K.D. and S.K.; resources, K.D., M.G., H.J.J., D.A.R. and K.K.; data curation, S.K.; writing—original draft preparation, S.K. and K.D.; writing—review and editing, K.D. and S.K.; visualization, S.K. and K.D.; supervision, K.D.; quision, K.D. All authors have read and agreed to the published version of the manuscript.

**Funding:** This research received no external funding.

**Institutional Review Board Statement:** Not applicable.

**Informed Consent Statement:** Not applicable.

**Data Availability Statement:** Data are available at this placeholder DOI: <https://doi.org/10.17863/CAM.73576>.

**Conflicts of Interest:** The authors declare no conflict of interest.

#### Appendix A

The conductivity of gold ( $\sigma_{Au}$ ) is described by the Drude model expression as

$$\sigma_{Au} = \varepsilon_0 \frac{\omega_p^2}{\gamma + i\omega} \quad (\text{A1})$$

where plasma frequency  $\omega_p$  is  $2\pi \times 2175$  THz and collision frequency  $\gamma$  is  $2\pi \times 6.5$  THz [1]. Here,  $\varepsilon_0$  is the vacuum electric constant. It should be noted that no temperature tuning is expected for the gold waveguide.

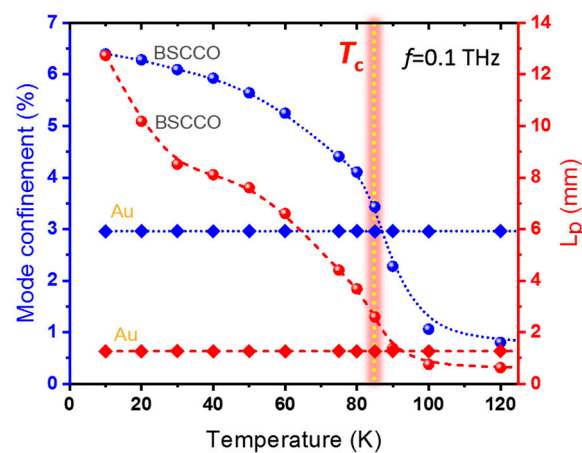


**Figure A1.** Mode confinement and propagation length of SPPs ( $L_p$ ) of BSCCO and gold plasmonic waveguide with structural size of  $h = 300$  nm and  $w = 300$  nm at  $f = 0.1$  THz. The vertical dashed line shows the  $T_c$  of BSCCO. Modal properties of gold waveguide are not dependent on temperature.

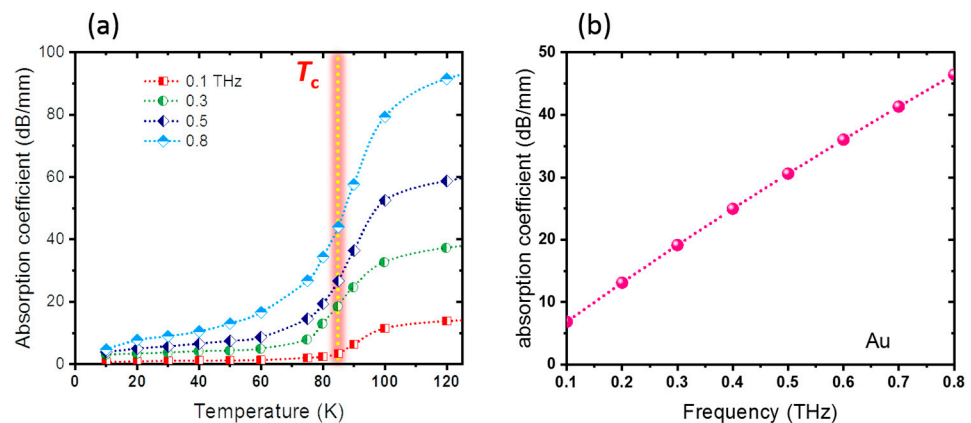


**Figure A2.** Absorption coefficient of (a) BSCCO plasmonic waveguide as a function of temperature at different frequencies. The vertical dashed line shows the  $T_c$  of BSCCO. (b) Gold plasmonic waveguide as a function of frequency. The absorption coefficient of the gold waveguide is temperature-independent.

## References

- Delfanazari, K.; Klemm, R.A.; Joyce, H.J.; Ritchie, D.A.; Kadowaki, K. Integrated, Portable, Tunable, and Coherent Terahertz Sources and Sensitive Detectors Based on Layered Superconductors. *Proc. IEEE* **2020**, *108*, 721–734. [[CrossRef](#)]
- Borodianskyi, E.A.; Krasnov, V.M. Josephson emission with frequency span 1–11 THz from small  $\text{Bi}_2\text{Sr}_2\text{CaCu}_2\text{O}_{8+\delta}$  mesa structures. *Nat. Commun.* **2017**, *8*, 1–7. [[CrossRef](#)]
- Ozyuzer, L.; Koshelev, A.E.; Kurter, C.; Gopalsami, N.; Li, Q.; Tachiki, M.; Kadowaki, K.; Yamamoto, T.; Minami, H.; Yamaguchi, H.; et al. Emission of coherent THz radiation from superconductors. *Science* **2007**, *318*, 1291–1293. [[CrossRef](#)] [[PubMed](#)]
- Ozyuzer, L.; Simsek, Y.; Koseoglu, H.; Turkoglu, F.; Kurter, C.; Welp, U.; Koshelev, A.E.; Gray, K.E.; Kwok, W.K.; Yamamoto, T.; et al. Terahertz wave emission from intrinsic Josephson junctions in high- $T_c$  superconductors. *Supercond. Sci. Technol.* **2009**, *22*, 114009. [[CrossRef](#)]
- Welp, U.; Kadowaki, K.; Kleiner, R. Superconducting emitters of THz radiation. *Nat. Photonics* **2013**, *7*, 702–710. [[CrossRef](#)]
- Tsujimoto, M.; Yamamoto, T.; Delfanazari, K.; Nakayama, R.; Kitamura, T.; Sawamura, M.; Kashiwagi, T.; Minami, H.; Tachiki, M.; Kadowaki, K.; et al. Broadly tunable subterahertz emission from Internal Branches of the current-Voltage characteristics of superconducting  $\text{Bi}_2\text{Sr}_2\text{CaCu}_2\text{O}_{8+\delta}$  single crystals. *Phys. Rev. Lett.* **2012**, *108*, 107006. [[CrossRef](#)] [[PubMed](#)]
- Klemm, R.A.; Delfanazari, K.; Tsujimoto, M.; Kashiwagi, T.; Kitamura, T.; Yamamoto, T.; Sawamura, M.; Ishida, K.; Hattori, T.; Kadowaki, K. Modeling the electromagnetic cavity mode contributions to the THz emission from triangular  $\text{Bi}_2\text{Sr}_2\text{CaCu}_2\text{O}_{8+\delta}$  mesas. *Phys. C* **2013**, *491*, 30–34. [[CrossRef](#)]



8. Delfanazari, K.; Asai, H.; Tsujimoto, M.; Kashiwagi, T.; Kitamura, T.; Yamamoto, T.; Sawamura, M.; Ishida, K.; Tachiki, M.; Klemm, R.A.; et al. Study of coherent and continuous terahertz wave emission in equilateral triangular mesas of superconducting  $\text{Bi}_2\text{Sr}_2\text{CaCu}_2\text{O}_{8+\delta}$  intrinsic Josephson junctions. *Phys. C Supercond. Appl.* **2013**, *491*, 16–19. [[CrossRef](#)]
9. Kitamura, T.; Kashiwagi, T.; Tsujimoto, M.; Delfanazari, K.; Sawamura, M.; Ishida, K.; Sekimoto, S.; Watanabe, C.; Yamamoto, T.; Minami, H.; et al. Effects of magnetic fields on the coherent THz emission from mesas of single crystal  $\text{Bi}_2\text{Sr}_2\text{CaCu}_2\text{O}_{8+\delta}$ . *Phys. C Supercond. Appl.* **2013**, *494*, 117–120. [[CrossRef](#)]
10. Delfanazari, K.; Asai, H.; Tsujimoto, M.; Kashiwagi, T.; Kitamura, T.; Yamamoto, T.; Sawamura, M.; Ishida, K.; Watanabe, C.; Sekimoto, S.; et al. Tunable terahertz emission from the intrinsic Josephson junctions in acute isosceles triangular  $\text{Bi}_2\text{Sr}_2\text{CaCu}_2\text{O}_{8+\delta}$  mesas. *Opt. Express* **2013**, *21*, 2171–2184. [[CrossRef](#)]
11. Kadowaki, K.; Tsujimoto, M.; Delfanazari, K.; Kitamura, T.; Sawamura, M.; Asai, H.; Yamamoto, T.; Ishida, K.; Watanabe, C.; Sekimoto, S.; et al. Quantum terahertz electronics (QTE) using coherent radiation from high temperature superconducting  $\text{Bi}_2\text{Sr}_2\text{CaCu}_2\text{O}_{8+\delta}$  intrinsic Josephson junctions. *Phys. C Supercond. Appl.* **2013**, *491*, 2–6. [[CrossRef](#)]
12. Delfanazari, K.; Asai, H.; Tsujimoto, M.; Kashiwagi, T.; Kitamura, T.; Ishida, K.; Watanabe, C.; Sekimoto, S.; Yamamoto, T.; Minami, H.; et al. Terahertz oscillating devices based upon the intrinsic Josephson junctions in a high temperature superconductor. *J. Infrared Millim. Terahertz Waves* **2014**, *35*, 131–146. [[CrossRef](#)]
13. Delfanazari, K.; Asai, H.; Tsujimoto, M.; Kashiwagi, T.; Kitamura, T.; Yamamoto, T.; Wilson, W.; Klemm, R.A.; Hattori, T.; Kadowaki, K. Effect of bias electrode position on terahertz radiation from pentagonal mesas of superconducting  $\text{Bi}_2\text{Sr}_2\text{CaCu}_2\text{O}_{8+\delta}$ . *IEEE Trans. Terahertz Sci. Technol.* **2015**, *5*, 505–511. [[CrossRef](#)]
14. Cercone, D.P.; Reid, C.; Doty, C.M.; Gramajo, A.; Campbell, T.D.; Morales, M.A.; Delfanazari, K.; Tsujimoto, M.; Kashiwagi, T.; Yamamoto, T.; et al. Cavity mode enhancement of terahertz emission from equilateral triangular microstrip antennas of the high-T<sub>c</sub> superconductor  $\text{Bi}_2\text{Sr}_2\text{CaCu}_2\text{O}_{8+\delta}$ . *J. Phys. Condens. Matter* **2017**, *29*, 015601. [[CrossRef](#)] [[PubMed](#)]
15. Kashiwagi, T.; Yamamoto, T.; Minami, H.; Tsujimoto, M.; Yoshizaki, R.; Delfanazari, K.; Kitamura, T.; Watanabe, C.; Nakade, K.; Yasui, T.; et al. Efficient Fabrication of Intrinsic-Josephson-Junction Terahertz Oscillators with Greatly Reduced Self-Heating Effects. *Phys. Rev. Appl.* **2015**, *4*, 054018. [[CrossRef](#)]
16. Kashiwagi, T.; Yamamoto, T.; Kitamura, T.; Asanuma, K.; Watanabe, C.; Nakade, K.; Yasui, T.; Saiwai, Y.; Shibano, Y.; Kubo, H.; et al. Generation of electromagnetic waves from 0.3 to 1.6 terahertz with a high-T<sub>c</sub> superconducting  $\text{Bi}_2\text{Sr}_2\text{CaCu}_2\text{O}_{8+\delta}$  intrinsic Josephson junction emitter. *Appl. Phys. Lett.* **2015**, *106*, 092601. [[CrossRef](#)]
17. Delfanazari, K.; Tsujimoto, M.; Kashiwagi, T.; Yamamoto, T.; Nakayama, R.; Hagino, S.; Kitamura, T.; Sawamura, M.; Hattori, T.; Minami, H.; et al. THz emission from a triangular mesa structure of Bi-2212 intrinsic Josephson junctions. *J. Phys. Conf. Ser.* **2012**, *400*, 022014. [[CrossRef](#)]
18. Delfanazari, K.; Asai, H.; Tsujimoto, M.; Kashiwagi, T.; Kitamura, T.; Sawamura, M.; Ishida, K.; Yamamoto, T.; Hattori, T.; Klemm, R.A.; et al. Experimental and theoretical studies of mesas of several geometries for terahertz wave radiation from the intrinsic Josephson junctions in superconducting  $\text{Bi}_2\text{Sr}_2\text{CaCu}_2\text{O}_{8+\delta}$ . In Proceedings of the 7th International Conference on Infrared, Millimeter, and Terahertz Waves, Wollongong, NSW, Australia, 23–28 September 2012; pp. 1–2. [[CrossRef](#)]
19. Kashiwagi, T.; Tsujimoto, M.; Yamamoto, T.; Minami, H.; Yamaki, K.; Delfanazari, K.; Deguchi, K.; Orita, N.; Koike, T.; Nakayama, R.; et al. High temperature superconductor terahertz emitters: Fundamental physics and its applications. *Jpn. J. Appl. Phys.* **2012**, *51*, 010113. [[CrossRef](#)]
20. Savinov, V.; Delfanazari, K.; Fedotov, V.A.; Zheludev, N.I. Giant sub-THz nonlinear response in superconducting metamaterial. In Proceedings of the CLEO:2014 Laser Science to Photonic Applications, San Jose, CA, USA, 8–14 June 2014; 2014; Volume SW3I-8, pp. 2–3. [[CrossRef](#)]
21. Klemm, R.A.; Davis, A.E.; Wang, Q.X.; Yamamoto, T.; Cercone, D.P.; Reid, C.; Koopman, M.L.; Minami, H.; Kashiwagi, T.; Rain, J.R.; et al. Terahertz emission from the intrinsic Josephson junctions of high-symmetry thermally-managed  $\text{Bi}_2\text{Sr}_2\text{CaCu}_2\text{O}_{8+\delta}$  microstrip antennas. *IOP Conf. Ser. Mater. Sci. Eng.* **2017**, *279*. [[CrossRef](#)]
22. Tsujimoto, M.; Minami, H.; Delfanazari, K.; Sawamura, M.; Nakayama, R.; Kitamura, T.; Yamamoto, T.; Kashiwagi, T.; Hattori, T.; Kadowaki, K. Terahertz imaging system using high-T<sub>c</sub> superconducting oscillation devices. *J. Appl. Phys.* **2012**, *111*, 123111. [[CrossRef](#)]
23. Delfanazari, K.; Klemm, R.A.; Tsujimoto, M.; Cercone, D.P.; Yamamoto, T.; Kashiwagi, T.; Kadowaki, K. Cavity modes in broadly tunable superconducting coherent terahertz sources. *J. Phys. Conf. Ser.* **2019**, *1182*, 012011. [[CrossRef](#)]
24. Kashiwagi, T.; Deguchi, K.; Tsujimoto, M.; Koike, T.; Orita, N.; Delfanazari, K.; Nakayama, R.; Kitamura, T.; Hagino, S.; Sawamura, M.; et al. Excitation mode characteristics in Bi2212 rectangular mesa structures. *J. Phys. Conf. Ser.* **2012**, *400*, 022050. [[CrossRef](#)]
25. Tsujimoto, M.; Yamamoto, T.; Delfanazari, K.; Nakayama, R.; Orita, N.; Koike, T.; Deguchi, K.; Kashiwagi, T.; Minami, H.; Kadowaki, K. THz-wave emission from inner I-V branches of intrinsic Josephson junctions in  $\text{Bi}_2\text{Sr}_2\text{CaCu}_2\text{O}_{8+\delta}$ . *J. Phys. Conf. Ser.* **2012**, *400*, 022127. [[CrossRef](#)]
26. Rahmonov, I.R.; Shukrinov, Y.M.; Zemlyanaya, E.V.; Sarhadov, I.; Andreeva, O. Mathematical modeling of intrinsic Josephson junctions with capacitive and inductive couplings. *J. Phys. Conf. Ser.* **2012**, *393*, 012022. [[CrossRef](#)]
27. Botha, A.E.; Rahmonov, I.R.; Shukrinov, Y.M. Spontaneous and Controlled Chaos Synchronization in Intrinsic Josephson Junctions. *IEEE Trans. Appl. Supercond.* **2018**, *28*, 1–6. [[CrossRef](#)]

28. Xiong, Y.; Kashiwagi, T.; Klemm, R.A.; Kadowaki, K.; Delfanazari, K. Engineering the Cavity modes and Polarization in Integrated Superconducting Coherent Terahertz Emitters. In Proceedings of the 2020 45th International Conference on Infrared, Millimeter, and Terahertz Waves (IRMMW-THz), Buffalo, NY, USA, 8–13 November 2020; pp. 1–2. [[CrossRef](#)]
29. Nakade, K.; Kashiwagi, T.; Saiwai, Y.; Minami, H.; Yamamoto, T.; Klemm, R.A.; Kadowaki, K. Applications using high-Tc superconducting terahertz emitters. *Sci. Rep.* **2016**, *6*, 1–8. [[CrossRef](#)]
30. Singh, R.; Zheludev, N. Superconductor photonics. *Nat. Photonics* **2014**, *8*, 679–680. [[CrossRef](#)]
31. Hayashi, S.; Okamoto, T. Plasmonics: Visit the past to know the future. *J. Phys. D Appl. Phys.* **2012**, *45*, 433001. [[CrossRef](#)]
32. Barnes, W.L.; Dereux, A.; Ebbesen, T.W. Surface plasmon subwavelength optics. *Nature* **2003**, *424*, 824–830. [[CrossRef](#)]
33. Ioannidis, T.; Gric, T.; Rafailov, E. Surface plasmon polariton waves propagation at the boundary of graphene based metamaterial and corrugated metal in THz range. *Opt. Quantum Electron.* **2020**, *52*, 1–12. [[CrossRef](#)]
34. Gric, T.; Wartak, M.S.; Cada, M.; Wood, J.J.; Hess, O.; Pistora, J. Spoof plasmons in corrugated semiconductors. *J. Electromagn. Waves Appl.* **2015**, *29*, 1899–1907. [[CrossRef](#)]
35. Tsiatmas, A.; Fedotov, V.A.; García De Abajo, F.J.; Zheludev, N.I. Low-loss terahertz superconducting plasmonics. *New J. Phys.* **2012**, *14*, 115006. [[CrossRef](#)]
36. Economou, E.N. Surface plasmons in thin films. *Phys. Rev.* **1969**, *182*, 539. [[CrossRef](#)]
37. Pracht, U.S.; Heintze, E.; Clauss, C.; Hafner, D.; Bek, R.; Werner, D.; Gelhorn, S.; Scheffler, M.; Dressel, M.; Sherman, D.; et al. Electrodynamics of the superconducting state in ultra-thin films at THz frequencies. *IEEE Trans. Terahertz Sci. Technol.* **2013**, *3*, 269–280. [[CrossRef](#)]
38. Kurter, C.; Abrahams, J.; Shvets, G.; Anlage, S.M. Plasmonic scaling of superconducting metamaterials. *Phys. Rev. B* **2013**, *88*, 180510. [[CrossRef](#)]
39. Wu, J.; Dai, H.; Wang, H.; Jin, B.; Jia, T.; Zhang, C.; Cao, C.; Chen, J.; Kang, L.; Xu, W.; et al. Extraordinary terahertz transmission in superconducting subwavelength hole array. *Opt. Express* **2011**, *19*, 1101–1106. [[CrossRef](#)]
40. Tsiatmas, A.; Buckingham, A.R.; Fedotov, V.A.; Wang, S.; Chen, Y.; De Groot, P.A.J.; Zheludev, N.I. Superconducting plasmonics and extraordinary transmission. *Appl. Phys. Lett.* **2010**, *97*, 111106. [[CrossRef](#)]
41. Ma, Y.; Eldlio, M.; Maeda, H.; Zhou, J.; Cada, M.; Zhai, X.; Wang, L.L.; Wang, L.L.; Lindquist, N.C.; Nagpal, P.; et al. Plasmonic properties of superconductor–insulator–superconductor waveguide. *Appl. Phys. Express* **2016**, *9*, 072201. [[CrossRef](#)]
42. Veronis, G.; Fan, S. Modes of subwavelength plasmonic slot waveguides. *J. Light. Technol.* **2007**, *25*, 2511–2521. [[CrossRef](#)]
43. Novotny, L.; Hecht, B. *Principles of Nano-Optics*; Cambridge University Press: Cambridge, UK, 2012; ISBN 9781107005464.
44. Kawano, K.; Kitoh, T. *INTRODUCTION to Optical Waveguide Analysis*; Wiley-Interscience: Hoboken, NJ, USA, 2004. [[CrossRef](#)]
45. Kalthor, S.; Ghanaatshoar, M.; Delfanazari, K. Guiding of terahertz photons in superconducting nano-circuits. In Proceedings of the 2020 International Conference on UK-China Emerging Technologies (UCET), Glasgow, UK, 20–21 August 2020; pp. 1–3. [[CrossRef](#)]
46. Corson, J.; Orenstein, J.; Oh, S.; O'Donnell, J.; Eckstein, J.N. Nodal quasiparticle lifetime in the superconducting state of  $\text{Bi}_2\text{Sr}_2\text{CaCu}_2\text{O}_{8+\delta}$ . *Phys. Rev. Lett.* **2000**, *85*, 2569–2572. [[CrossRef](#)] [[PubMed](#)]
47. Mallozzi, R.; Corson, J.; Orenstein, J.; Eckstein, J.N.; Bozovic, I. Terahertz conductivity and c-axis plasma resonance in  $\text{Bi}_2\text{Sr}_2\text{CaCu}_2\text{O}_{8+\delta}$ . *J. Phys. Chem. Solids* **1998**, *59*, 2095–2099. [[CrossRef](#)]
48. Kalthor, S.; Ghanaatshoar, M.; Kashiwagi, T.; Kadowaki, K.; Kelly, M.J.; Delfanazari, K. Thermal Tuning of High-Tc Superconducting  $\text{Bi}_2\text{Sr}_2\text{CaCu}_2\text{O}_{8+\delta}$  Terahertz Metamaterial. *IEEE Photonics J.* **2017**, *9*, 1–8. [[CrossRef](#)]
49. Barnes, W.L. Surface plasmon-polariton length scales: A route to sub-wavelength optics. *J. Opt. A Pure Appl. Opt.* **2006**, *8*, S87–S93. [[CrossRef](#)]
50. Tian, Z.; Singh, R.; Han, J.; Gu, J.; Xing, Q.; Zhang, W. Terahertz superconducting plasmonic hole array. *Opt. Lett.* **2010**, *35*, 3586–3588. [[CrossRef](#)] [[PubMed](#)]
51. Maier, S.A. *Plasmonics Fundamentals and Applications*; Springer Science & Business Media: Berlin, Germany, 2007; ISBN 9780387331508.
52. Ono, M.; Hata, M.; Tsunekawa, M.; Nozaki, K.; Sumikura, H.; Chiba, H.; Notomi, M. Ultrafast and energy-efficient all-optical switching with graphene-loaded deep-subwavelength plasmonic waveguides. *Nat. Photonics* **2020**, *14*, 37–43. [[CrossRef](#)]